Lithium-storage and cycleability of nano-CdSnO$_3$ as an anode material for lithium-ion batteries

Yogesh Sharma, N. Sharma, G.V. Subba Rao, B.V.R. Chowdari *

Department of Physics, National University of Singapore, 117542, Singapore

ABSTRACT

Nano-CdSnO$_3$ is prepared by thermal decomposition of the precursor, CdSn(OH)$_6$ at 600 °C for 6 h in air. The material is characterized physically by X-ray diffraction (XRD), high-resolution transmission electron microscopy (HR-TEM) and selected-area electron diffraction (SAED) techniques. Nano-CdSnO$_3$ exhibits a reversible and stable capacity of 475($\pm$5) mAh g^{-1} ($\sim$5 mol of cycleable Li per mole of CdSnO$_3$) for at least 40 cycles between 0.005 and 1.0 V at a current rate of 0.13 C. Extensive capacity fading is found when cycling in the range 0.005–1.3 V. Cyclic voltammetry studies complement galvanostatic cycling data and reveal average discharge and charge potentials of 0.2 and 0.4 V, respectively. The proposed reaction mechanism is supported by ex situ XRD, TEM and SAED studies. The electrochemical impedance spectra taken during 1st and 10th cycle are fitted with an equivalent circuit to evaluate impedance parameters and the apparent chemical diffusion coefficient (D_{Li^+}) of Li. The bulk impedance, R_b, dominates at low voltages ($\leq$0.25 V), whereas the combined surface film and charge-transfer impedance ($R_{(sf+ct)}$) and the Warburg impedance dominate at higher voltages, $\geq$0.25 V. The D_{Li^+} is in the range of (0.5–0.9) $\times$ 10^{-13} cm^2 s^{-1} at V = 0.5–1.0 V during the 10th cycle.

1. Introduction

Presently, fossil fuels are being used for most automobile vehicles, but natural sources of these fuels are limited. Therefore, extensive research is in progress to search for alternatives to replace, partly or fully, fossil fuels. Hydrogen-based fuel cells, solar cells and rechargeable batteries of high specific energy are some of the alternatives [1–3]. The lithium-ion batteries (LIBs) have fulfilled the energy requirement successfully for low-power consumer portable appliances such as laptop computers, mobile phones and camcorders [1,3–6]. For hybrid vehicles, space and military applications, research on LIBs are targeted towards improving energy and power performance, longevity, and safety in operation [1–6]. Many of the above parameters depend significantly up on the nature of electrode materials and electrolyte used in LIBs. Typically, a LIB consists of LiCoO$_2$ as the positive electrode (cathode) and specialty graphite as the negative electrode (anode). New anode materials are expected to achieve higher capacities than that of graphite (theoretical capacity: 372 mAh g^{-1}) [1–6].

Oxides based on tin (Sn) or cobalt (Co) have been investigated extensively as anode materials since they can deliver 2–3 times the capacity of graphite [6–16]. Co-based oxides display their maximum capacity at a higher potential ($\sim$2.0 V) versus Li. This drawback makes them unsuitable for LIBs of specific energy in present designs that employ 4 V-cathodes like LiCoO$_2$ and liquid/gel electrolytes [1,3–6,9–12]. On the other hand, Sn-based compounds have an average charge potential of $\sim$0.5 V versus Li and thus can be considered as the suitable candidates for anode materials. These compounds, however, are subject to the serious problem of volume variation in the unit cell by up to 300%, on cycling, since the reaction mechanism involves the formation and decomposition of Li$_{4.4}$Sn alloy [1,3–6,13–18]. This leads to capacity fading on long-term cycling due to crumbling and cracking of the electrode material that, in turn, cause electronic isolation from the current collector. In recent years, the capacity fading of Sn-oxides has been suppressed to some extent by using nano-sized active material [1,3–6,14–17], and/or some matrix element [14,19–27] that can buffer the volume variation during repeated cycling, and by restricting lithium cycling to an appropriate voltage window [1,4,14,20].

A number of Sn-based oxides, namely, ASnO$_3$ (A = Ca, Sr, Ba) [14,19,26], M$_2$SnO$_4$ (M = Mg, Mn, Co, Zn) [22,23,28], SnP$_2$O$_7$ [21] and Sn$_2$BPO$_6$ [20,21] have been investigated as anode materials for LIBs. In these cases, the alkaline earth ions and the phosphate/boro-phosphate anions do not participate in cycling and remain electrochemically inactive in the form of oxides (e.g.,

* Corresponding author. Tel.: +65 6516 2531; fax: +65 6777 6126.
E-mail addresses: yogeshsharma@nus.edu.sg (Y. Sharma), phyns@nus.edu.sg (N. Sharma), phyvsg@nus.edu.sg (G.V. Subba Rao), phychowd@nus.edu.sg (B.V.R. Chowdari).

CaO) and Li-phosphates. Nevertheless, studies have shown that these inactive matrix components do have an impact on the overall lithium cycleability of the Sn-based oxides.

Electrochemically active matrix elements like Zn and Cd in conjunction with Sn can be considered as good host materials without sacrificing the overall gravimetric capacity, since they can also form an alloy with Li, in addition to Sn [23,24,28,29]. Belliard et al. [23,24] studied the lithium cycleability of crystalline Zn_2SnO_4 with a spinel structure and the composites $ZnO \cdot SnO_2$ and $ZnO \cdot 2SnO_2$ that were obtained by ball milling of the respective binary oxides. Zn_2SnO_4 [23] showed a first cycle reversible capacity of 550 mAh g^{-1} in the voltage window 0.02–1.5 V versus Li. For $ZnO \cdot SnO_2$ and $ZnO \cdot 2SnO_2$ (20 h ball-milled) [24], the respective capacity values were 548 and 613 mAh g^{-1} in the voltage window 0.02–1.0 V. Both the capacities degraded to ~50% after 10 discharge–charge cycles. Rong et al. [28] studied the lithium cyclability of the crystalline Zn_2SnO_4 prepared by hydrothermal method. When cycled in the voltage window, 0.05–3.0 V at a current rate of 100 mA g^{-1}, the cube-shaped-Zn_2SnO_4 (size 30–400 nm) exhibited an initial reversible capacity of 988 mAh g^{-1}, but slow capacity fading (0.8% per cycle) was noted over 50 cycles. The cycling performance of 'irregular-sized' Zn_2SnO_4 was found to be slightly inferior to that of the 'cube-shaped' material.

The compound, $CdSnO_3$ is comprised of two cations that are electrochemically active towards Li and is extensively studied as a gas sensing material [30,31]. Cadmium can consume 3 mol of Li to form the alloy Li_3Cd and thereby contribute to reversible capacity in addition to 4.4 mol of Li for the Sn-alloy. As a result, the theoretical reversible capacity of $CdSnO_3$ is as high as 711 mAh g^{-1}. The above-mentioned fact provides motivation to evaluate its suitability as an anode material for LIBs. As mentioned earlier, the cube-shaped morphology of Zn_2SnO_4 was found to be favourable for lithium cycling [28]. Therefore, in the present work, the cube shape morphology of nano-$CdSnO_3$ is obtained by a thermal decomposition method and characterized by various physical techniques. Lithium cycleability studies show that ~5 mol of Li per mole of $CdSnO_3$ are cycleable with a capacity of 475(±5) mAh g^{-1} stable up to 40 cycles. Complementary data from cyclic voltammetry, impedance spectral, ex situ X-ray diffraction (XRD) and transmission electron microscope are reported and discussed.

2. Experimental

The metal chlorides $CdCl_2 \cdot H_2O$ (0.03 mol, Merck; >98%) and $SnCl_4$ (0.03 mol, Merck; >99%) were dissolved separately in de-ionized water and then mixed together. A white precipitate of $CdSn(OH)_6$ was obtained when LiOH (0.2 mol, Merck; ~98%) solution was added drop-wise to the warm (~50 °C) mixed chloride solution. The precipitate was recovered by filtration and washed several times with de-ionized water to remove any chloride impurity. It was dried at 100 °C for 12 h and then calcined in air in two batches, one at 400 °C and the other at 600 °C, for 6 h followed by cooling to room temperature. The compounds were preserved in a desiccator.

Structural and morphological characterizations were performed by means of an X-ray diffractometer (Philips, Expert) equipped with Cu Kα radiation, transmission electron microscopy (TEM) (JEOL JEM 2100 operating at 200 kV) and selected-area electron diffraction (SAED) studies. The doctor-blade technique was used to prepare a composite electrode for electrochemical studies. Etched Cu-foil (thickness ~10 μm) was used as the current-collector. The electrode contained 70:15:15 weight ratio of the active material, Super P carbon (MMM Ensaco) and binder (Kynar 2801), respectively. The mass of the active material and the effective area of electrode were ~3 mg and ~2 cm^2, respectively. Coin-type cells (2016; diameter, 20 mm, thickness, 1.6 mm) were fabricated in an Ar-filled glove box

(MBraun, Germany) with lithium metal as the counter electrode, 1 M $LiPF_6$ dissolved in ethylene carbonate (EC) and diethyl carbonate (DEC) (1:1 by volume; Merck, Selectipur LP 40) as the electrolyte and glass micro-fibre filter (Whatman) as the separator. Details of cell and electrode preparation are described in our earlier reports [12,14,25,26].

Cyclic voltammetry and galvanostatic charge–discharge cycling of the cells were carried out at room temperature, after ageing for 12 h (to ensure the percolation of the electrolyte in to the electrode material), by means of a Macpile II (Biologic, France) and computer controlled Bitrode multiple battery tester (model SCN, Bitrode, USA), respectively. Electrochemical impedance spectroscopy was performed with a Solartron impedance/phase-gain analyzer (SI 1255) coupled to a battery testing unit (1470). The measurements were carried out at room temperature in the frequency range 5 mHz to 0.10 MHz, with an ac signal of amplitude 5 mV. Data acquisition and analysis were undertaken, respectively, with the impedance software, Zplot and Zview (version 2.2, Scribner Associates, Inc., USA). For ex situ XRD, TEM and SAED analyses, the composite electrode was recovered from the cell inside a glove box (O_2 and H_2O content <1 ppm) and washed thoroughly with DEC to remove electrolyte and processed as described in our earlier reports [12,14].

3. Results and discussion

3.1. Structural and morphological characterization

X-ray diffraction patterns of as-prepared $CdSn(OH)_6$, and of those heated at 400 and 600 °C for 6 h each, are shown in Fig. 1. The XRD pattern of the as-prepared mixed hydroxide shows a phase-pure form with a cubic crystal structure and matches well with the pattern reported in literature [32]. The derived lattice parameter, $a = 8.02(2)$ Å is in good agreement with $a = 8.00$ Å given in the JCPDS card no. # 28-0202. The XRD pattern the $CdSn(OH)_6$ heated at 400 °C for 6 h is devoid of any peak and shows only broad humps at $2\theta \sim 32°$ and $\sim 55°$, which indicates its amorphous nature. On the other hand, the pattern of the precursor heated at 600 °C for 6 h clearly shows the characteristic peaks of rhombohedral–hexagonal $CdSnO_3$ and was found to be orange-yellow in colour. The XRD pattern (Fig. 1) matches well with that reported by Zhang et al. [30] and Liu et al. [31] who obtained $CdSnO_3$ by thermal
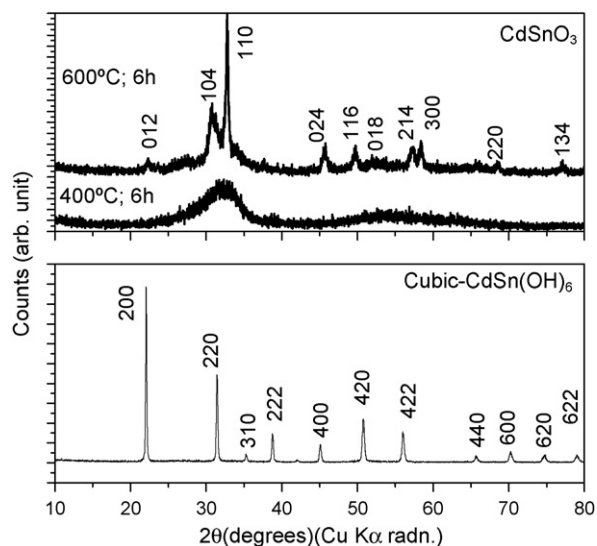

Fig. 1. X-ray diffraction (XRD) patterns of as-prepared $CdSn(OH)_6$ and of products calcined in air at 400 and 600 °C for 6 h. Miller indices ($h\,k\,l$) are shown.
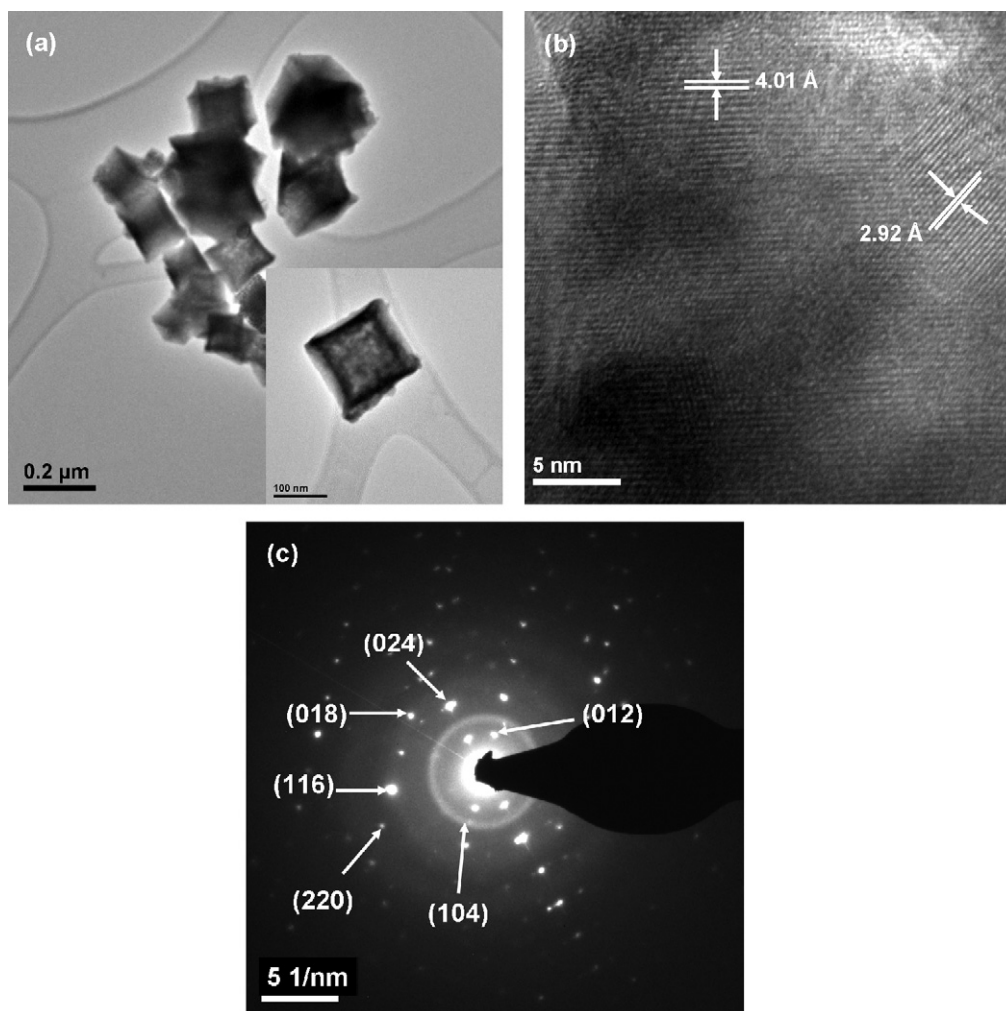
Fig. 2. (a) TEM image of nano-CdSnO$_3$ showing cubic morphology. Inset shows a single cube containing agglomerated nano-particles. Scale bars are 200 and 100 nm, respectively. (b) HR-TEM lattice image of nano-CdSnO$_3$, obtained by heating precursor CdSn(OH)$_6$ in air at 600 °C for 6 h. Measured interplanar distances (d-values) from lattice fringes are shown. Scale bar is 5 nm. (c) SAED pattern. The different diffuse spots/rings are assigned to Miller indices of hexagonal-CdSnO$_3$. Scale bar is 5 nm^{-1}.

decomposition of a carbonate precursor and a hydroxide precursor, respectively. The hexagonal lattice parameters $a = 5.432$ Å and $c = 14.901$ Å are obtained by refining the XRD data using Rietveld refinement software TOPAS R2 (version 2.1). These values agree well with $a = 5.452$ Å and $c = 14.947$ Å given in the JCPDS card no. # 34-0758. The crystallite size of CdSnO$_3$ is estimated using Scherrer's equation, $P = K\lambda/(\beta_{1/2} \cos\theta)$ [14]. Here, K is a constant = 0.9, λ is the wavelength of Cu Kα radiation in Å (=1.54059) and $\beta_{1/2}$ is the full-width at half maximum (FWHM) of the maximum intensity peak (1 1 0) of the XRD pattern (Fig. 1) and θ is the scattering angle. The value of $\beta_{1/2}$ is calculated to be 0.24° after subtracting the instrumental broadening of 0.15°, which is estimated by using the standard compounds LiNbO$_3$ and LiCoO$_2$. The obtained value of $P = 30(\pm5)$ nm establishes the nano-particle nature of CdSnO$_3$.

The morphology of CdSnO$_3$ was investigated by TEM (Fig. 2a and the inset). An agglomeration of fine particles in nano-cube morphology is observed. A similar cubic-morphology was also observed by Tang et al. [32]. The high-resolution (HR) TEM lattice image and the SAED pattern (Fig. 2b and c) complement the XRD data and establish its ilmenite-type hexagonal crystal structure. As can be seen in Fig. 2b, the lattice planes with interplanar distances (d-values), $4.01(\pm0.02)$ Å and $2.92(\pm0.02)$ Å can be assigned to the (0 1 2) and (1 0 4) planes of hexagonal-CdSnO$_3$. The SAED pattern (Fig. 2c) shows diffuse spots overlapping with diffuse rings, which

indicate the nano-phase nature of CdSnO$_3$. The d-values that correspond to the spots/rings (Fig. 2c) are derived and the assigned Miller indices ($h\,k\,l$) correspond to different interplanar distances of hexagonal-CdSnO$_3$ within (±0.02) Å.

3.2. Electrochemical studies

3.2.1. Galvanostatic cycling

Galvanostatic cycling studies were performed on nano-CdSnO$_3$ at a constant current of 60 mA g^{-1} in two voltage windows, namely, 0.005–1.0 V and 0.005–1.3 V versus lithium metal. The initial reaction commences from the open-circuit voltage (OCV ~2.2 V) to deep discharge, 0.005 V. The results are shown in Fig. 3a in the form of voltage versus capacity profiles for the first discharge and charge cycle with upper cut-off voltages of 1.0 and 1.3 V. The profiles from the 2nd to the 30th cycle in the voltage range, 0.005–1.0 V are presented in Fig. 3b. For clarity, only selected cycles are given. The first discharge profile shows a voltage plateau region at 1.45 V, followed by a sloping profile until $530(\pm20)$ mAh g^{-1} (consumption of ~5.5 mol of Li per mole of CdSnO$_3$). This is attributed to structure destruction or the crystal lattice amorphisation reaction, in which nano-CdSnO$_3$ reacts with Li to form nano-sized Cd and Sn metal particles embedded in a Li$_2$O matrix. This is in accordance with the mechanism proposed earlier for several Sn-oxides (Eq.
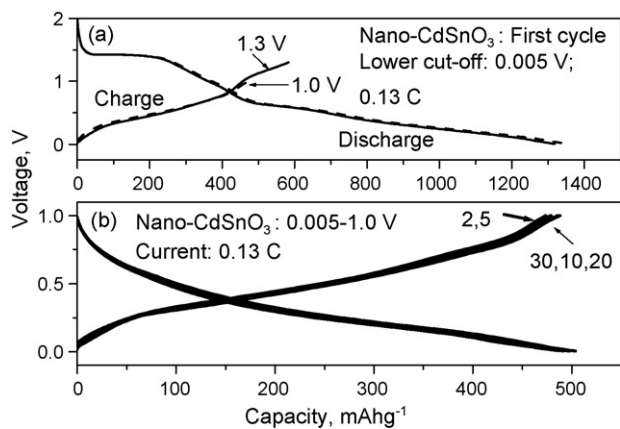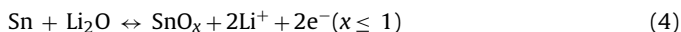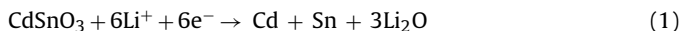
Fig. 3. Voltage vs. capacity profiles of nano-CdSnO$_3$–Li system at 60 mA g^{-1} (0.13 C) and room temperature. (a) First cycle in two-voltage windows, viz., 0.005–1.0 V (broken line) and 0.005–1.3 V (continuous line). (b) Profiles of 2–30 cycles in voltage window, 0.005–1.0 V. Only selected cycles are shown for clarity. Numbers refer to cycle number.

Fig. 4. Capacity vs. cycle number plots of nano-CdSnO$_3$–Li system at 60 mA g^{-1} (0.13 C) in voltage range (a) 0.005–1.0 V and (b) 0.005–1.3 V. Voltage windows are indicated. Filled and open symbols represent discharge and charge capacities, respectively. C-value is calculated assuming 1 C = 475 mA g^{-1}.

(1)) [1,4–6,14,15,19–28]. The voltage plateau and sloping regions indicate the two-phase and single-phase reactions, respectively:

$$CdSnO_3 + 6Li^+ + 6e^- \rightarrow Cd + Sn + 3Li_2O \qquad (1)$$

$$Cd + 3Li^+ + 3e^- \leftrightarrow Li_3Cd \qquad (2)$$

$$Sn + 4.4Li^+ + 4.4e^- \leftrightarrow Li_{4.4}Sn \qquad (3)$$

$$Sn + Li_2O \leftrightarrow SnO_x + 2Li^+ + 2e^- (x \leq 1) \qquad (4)$$

As per Eq. (1), theoretically, 6.0 mol of Li are consumed in the formation of the metals after the structure destruction reaction, and the observed value of 5.5 mol is quite close to this. The first discharge profile shows a minor voltage plateau region at ∼0.6 V, followed by a gradual sloping region extending to the lower cut-off voltage, 0.005 V. The overall first discharge capacity is 1330(±20) mAh g^{-1} (consumption of 13.9 mol of Li). The minor plateau region at 0.6 V is ascribed to intermediate LiCd$_3$ alloy formation which then merges with Li$_{4.4}$Sn formation and subsequently Li$_3$Cd formation (Eqs. (2) and (3)). The formation of Li$_3$Cd through intermediate alloy phases is supported by coulometric titration studies of the Li–Cd alloy system investigated by Huggins and co-workers [29]. The Li$_{4.4}$Sn alloy formation at ∼0.25 V is very well studied and documented in the literature for a number of binary and ternary tin oxide systems [1,4–6,15–27]. The observation here of slight differences in the voltage plateau positions as compared with the literature reports on Li–Cd and Li–Sn alloy systems are due to their dependence on the compound morphology, matrix element, crystal structure and the oxygen-coordination of the metal ion [1,14,15,19–26]. The theoretical capacity value of 13.4 mol of Li is quite close to the experimentally observed value of 13.9 mol of Li for the first discharge reaction. The slight excess consumption of 0.5 mol of Li can be ascribed to formation of a solid electrolyte interphase (SEI) at the electrode|electrolyte interface [4–6,14–16,25,26].

The first charge reaction involves the extraction of Li from the system up to 1.0 V and shows a sloping voltage profile and a capacity of 475(±5) mAh g^{-1} (∼5.0 mol of Li per mole of CdSnO$_3$). The underlying reaction mechanism is the de-alloying of Li$_3$Cd and Li$_{4.4}$Sn that releases Cd- and Sn-metal particles according to the reverse reactions given by Eqs. (2) and (3), respectively [1,4,5,13,14,29]. The theoretical value of charge capacity corresponds to 7.4 mol of Li. By contrast, the experimentally observed value is only ∼5 mol of Li and indicates that the de-alloying reaction is not complete, due to some type of 'mixed cation effect' and large unit-cell volume changes involved in the process. The 'mixed cation effect' may be defined as
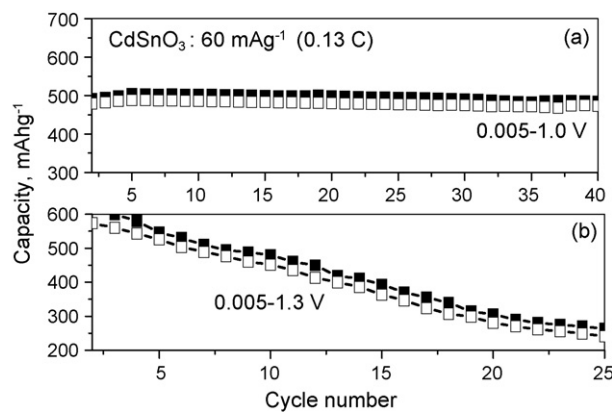
the effect of Cd on the de-alloying–alloying reactions of Sn and vice versa, thereby preventing the completion of the reverse reactions of Eqs. (2) and (3). It should be noted that there may also be some possibility of (Cd–Sn) alloy formation after the completion of the Eq. (1), and the Li-cycleability of the (Cd–Sn) alloy may be different from that of pure Cd and Sn metals. Indeed, the existence of alloys (Cd$_{0.05}$Sn$_{0.95}$) [33] and (Cd$_{0.3}$Sn$_{0.7}$) [34] has been documented in the literature. In any case, detailed studies are needed to clarify the 'mixed cation effect' in the present system.

The second discharge profile in the range of 0.005–1.0 V displays a capacity of 480(±5) mAh g^{-1} (∼5 mol of Li), i.e., almost identical to first charge capacity (Fig. 3b). The second charge profile is identical to the first charge profile and thereby indicates good reversibility of Eqs. (2) and (3). This is also shown by the voltage–capacity profiles in the range of 2–30 cycles (Fig. 3b). The capacity versus cycle number plot (Fig. 4a) shows that a stable capacity of 475(±5) mAh g^{-1} is maintained between 2 and 40 cycles at a current rate of 60 mA g^{-1} (0.13 C, assuming 1 C = 475 mAh g^{-1}). The average discharge and charge reaction potentials are 0.2 and 0.4 V, respectively, and the coulombic efficiency (η) between discharge and charge capacities is 97–98% in the range of 2–40 cycles.

The effect of increasing the upper cut-off voltage to 1.3 V on the cycling response of nano-CdSnO$_3$ was examined in a duplicate cell. The first discharge and charge profiles, shown in Fig. 3a, overlap very well with those obtained with a 1.0-V cut off voltage and therefore indicates good reproducibility of the electrode behaviour. With an upper cut-off voltage of 1.3 V, the first charge capacity is 580(±5) mAh g^{-1} (∼6.0 mol of Li), i.e., a higher value in comparison with 475(±5) mAh g^{-1} observed with a cut-off voltage of 1.0 V. Nevertheless, the reversible capacity degraded significantly on cycling and at the end of the 25th cycle, a capacity of 245(±5) mAh g^{-1} (∼2.6 mol of Li) is observed (Fig. 4b). This capacity fading can be attributed to SnO formation via the 'conversion reaction' shown in Eq. (4) and the associated volume changes [14,35,36]. Thus, the buffering ability of Li$_2$O to keep Sn-metal particles isolated from each other is drastically affected and leads to the observed capacity fading. Formation of CdO, in addition to SnO, on cycling to 1.3 V in the nano-CdSnO$_3$–Li system can be ruled out since studies by Li et al. [37], and our selves (unpublished) have shown that in the CdO–Li system, after the first discharge with lithium metal, CdO re-formation occurs only at ∼2.0 V. Hence, it is concluded that the favourable voltage range for cycling in the present case is 0.005–1.0 V, which yields a stable and reversible capacity of 475(±5) mAh g^{-1} (∼5 mol of cyclable Li) (Fig. 4a).
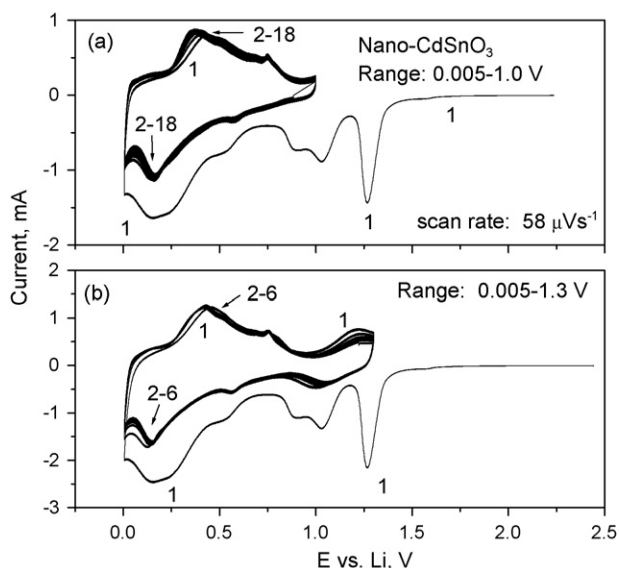
Fig. 5. Cyclic voltammograms (CVs) of nano-CdSnO₃ in potential window (a) 0.005–1.0 V and (b) 0.005–1.3 V vs Li at slow scan rate of 58 μV s⁻¹. Numbers refer to cycle number.

Fig. 6. Ex situ XRD patterns of electrode of bare nano-CdSnO₃, and of those discharged to 0.5 and 0.005 V vs. Li. Lines due to Cu-substrate and sample holder (Al) are indicated. Miller indices ($h\,k\,l$) are shown. The y-axis values are normalized for better comparison of XRD patterns.

3.2.2. Cyclic voltammetry

To discern the voltages at which discharge–charge reactions take place and to complement the galvanostatic cycling performance, cyclic voltammetry studies were performed on nano-CdSnO₃ versus Li at a slow sweep rate of 58 μV s⁻¹ in two different voltage windows, viz., 0.005–1.0 V and 0.005–1.3 V. The cyclic voltammograms (CVs) are presented in Fig. 5, in which the first discharge commences from the OCV of 2.3 V. An intense cathodic peak at 1.25 V is seen and can be ascribed to destruction of the crystal structure (amorphisation of lattice) through reduction of nano-CdSnO₃ to form nano-particles of Cd and Sn metals embedded in the Li₂O matrix (Eq. (1)). This is followed by a split peak at ∼1.0 and ∼0.9 V that can be ascribed to the formation of Li–Cd alloy (Eq. (2)) in stages [29]. Thereafter, a shoulder peak at ∼0.5 V and a broad peak at ∼0.1 V are observed which can be attributed to the complete formation of Li₃Cd and Li₄.₄Sn alloys (forward reactions of Eqs. (2) and (3)) [14,25–29]. The first anodic scan has a broad peak at ∼0.4 V and a low-intensity, but a well-defined peak at 0.75 V. These can be ascribed to the de-alloying reactions to give Sn and Cd metal particles, respectively (reverse reactions of Eqs. (2) and (3)) [14,25–29]. The second cathodic sweep displays various peaks that are attributable to the formation of Li–Cd and Li–Sn alloys at the same potentials as in the first cathodic sweep. Similarly, the second anodic sweep is a duplication of the first anodic sweep. The CVs, up to 18 cycles, overlap very well which indicates good lithium cycleability (Fig. 5a). The peak positions observed in the CV show the average discharge and charge potential to be 0.2 and 0.4 V, respectively. These values match well with the voltage plateau positions found in the galvanostatic capacity–voltage profiles in Fig. 3b.

The first cathodic sweep in the CV of nano-CdSnO₃ in the potential range 0.005–1.3 V and shown in Fig. 5b is identical to that in Fig. 5a. This demonstrates the excellent reproducibility of the duplicate cell. Nevertheless, an anodic peak at ∼1.2 V is clearly seen in the first charge curve (Fig. 5b). During 2nd to 6th cycles, the anodic peak persists at ∼1.2 V and the corresponding cathodic peak is seen at ∼1.1 V. These two peaks can be ascribed to the conversion reactions involving Li₂O and Sn-nano-particles (Eq. (4)) [14,35,36,38]. The occurrence of Eq. (4) is detrimental to long-term cycling because it gives rise to capacity fading, as has been noted from the galvanostatic cycling data (Fig. 4b). It is worth mentioning
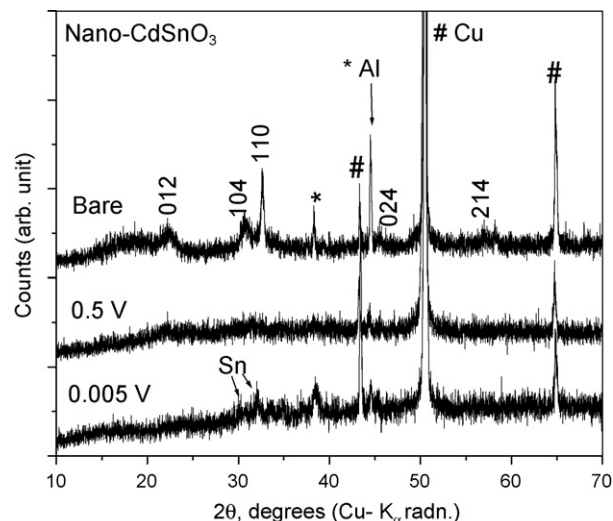
that studies on nano-composite 'CaO·SnO₂' and nano-CaSnO₃ [14] revealed that cycling to an upper cut-off voltage of 1.3 V versus Li gives rise to capacity fading. Therefore, it is concluded that the CV results corroborate the galvanostatic cycling data that the optimum voltage window for lithium cycling in nano-CdSnO₃ is 0.005–1.0 V (Figs. 3–5).

3.3. Ex situ XRD and TEM studies

Ex situ XRD studies were performed to supplement the galvanostatic cycling and cyclic voltammetry data. Duplicate cells were fabricated and cycled to a specific voltage and then aged for 2–3 h at that voltage. They were dismantled inside a glove box and the composite electrode was recovered, washed with the solvent (DEC) to remove the electrolyte, and finally used for ex situ studies. The XRD patterns of the bare electrode and of those discharged to voltages 0.5 and 0.005 V during first discharge are shown in Fig. 6. The characteristic peaks of the hexagonal-CdSnO₃ observed with the bare composite electrode disappear at 0.5 V, and only the peaks due to the substrate (Cu) and sample holder (Al) are seen. This observation indicates amorphisation of the lattice, and is in accordance with the galvanostatic cycling, CV data and the proposed reaction mechanism. In the XRD pattern of the fully discharged electrode (0.005 V), low-intensity peaks attributable to Sn-metal are seen. In accordance with the forward reaction of Eqs. (2) and (3), however, only the peaks due to Li₄.₄Sn and Li₃Cd alloys are expected. The presence of Sn-metal can possibly be attributed to the decomposition of (Li–Sn) alloy under exposure to air during sample loading and exposure to the X-rays.

Ex situ TEM and SAED studies were performed on the composite electrode in the charged state (1.0 V) after 15 cycles, results are presented in Fig. 7. The lattice image shows the presence of nanocrystalline regions, of size 3–6 nm, dispersed in the amorphous regions of Li₂O (Fig. 7a). The measured interplanar distances (d-values) are 2.84(±0.03) Å, 2.53(±0.03) Å and 2.32(±0.03) Å. The first value can be attributed to the (1 0 1) plane of tetragonal Sn metal (JCPDS card no. # 04-0673) and/or (0 0 2) plane of hexagonal Cd (JCPDS card no. # 85-1328). The latter two values can be assigned to the (1 0 0) and (1 0 1) planes of hexagonal-Cd metal, respectively.

The SAED pattern shows diffuse rings with the occasional diffuse spots that indicate the presence of nano-crystalline and amorphous
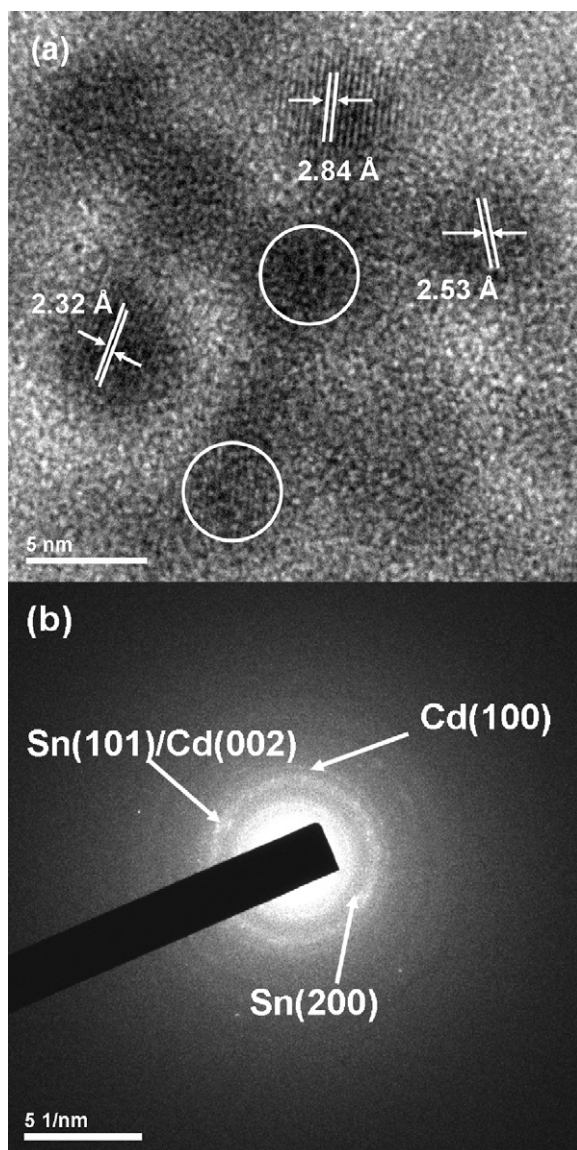
Fig. 7. Ex situ TEM of nano-CdSnO$_3$ charged to 1.0 V vs. Li after 15 cycles. (a) Lattice image. Nano-crystalline regions (3–6 nm) dispersed in amorphous regions are seen. Measured interplanar distances (d-values), 2.84($\pm$0.03) Å, 2.53($\pm$0.03) Å and 2.32($\pm$0.03) Å are assigned to tetragonal-Sn and hexagonal-Cd metals (see text). Circled regions show overlapping of planes of crystalline metallic Sn and Cd. Scale bar is 5 nm. (b) SAED pattern. Miller indices corresponding to diffuse spots/rings are assigned to metallic Sn and Cd. Scale bar is 5 nm^{-1}.

regions of the active material in the electrode (Fig. 7b). The d-values were derived by measuring the distance of spots/rings from the centre. They are: 2.93($\pm$0.03) Å, 2.81($\pm$0.03) Å and 2.54($\pm$0.03) Å. The first value can be assigned to the (2 0 0) plane of tetragonal Sn. The second and third values are close to the values observed in the lattice image (Fig. 7a) and thus belong to Sn and/or Cd metal. Therefore, on the basis of ex situ XRD, TEM and SAED studies, it is concluded that destruction of the crystal structure occurs during the first discharge. The products, formed on charging the electrode to 1.0 V after 15 cycles, are Sn and Cd metal. These findings support the proposed forward reaction of Eq. (1) and the reverse reactions of Eqs. (2) and (3).

3.4. Electrochemical impedance spectroscopy (EIS)

The electrode reaction kinetics of a number of cathode and anode materials for LIBs has been studied by EIS technique. This technique can be used as a supplementary study to complement the galvanostatic and cyclic voltammetry data. Binary and ternary oxide anode materials such as SnO [38], nano-CaO·SnO$_2$ [14], Co$_3$O$_4$ [39] and FeCo$_2$O$_4$ [10] have been evaluated by impedance analysis. The EIS technique was used to study the reaction kinetics of nano-CdSnO$_3$ in a coin cell configuration versus Li during 1st and 10th cycles. The cell was discharged from OCV to selected voltages during the first cycle, relaxed for 2 h, and then impedance data were collected. The cell was again subjected to nine cycles (range, 0.005–1.0 V at 60 mA g^{-1}) and data were collected during the 10th cycle at selected voltages. Impedance measurements were carried out in the frequency range of 0.1 MHz to 5 mHz and the data were plotted in the form of Nyquist plots (Z' vs. Z'') where Z' and Z'' refer to the real and imaginary parts of the cell impedance, respectively (Fig. 8). The equivalent electrical circuit, which was used to fit the impedance data, is shown in Fig. 9. The theoretical circuit consists of series and parallel combinations of resistances (R) and constant-phase elements (CPEs). The CPEs are used instead of the pure capacitors due to occurrence of depressed semicircles in the Nyquist plots, that indicate a deviation from ideal capacitor behaviour. The impedance of CPE can be derived from the equation, $Z_{CPE} = 1/[C_i(j\omega)^n]$ where $j = \sqrt{-1}$, ω is the angular frequency, C_i is the capacitance, and n is a constant. The value of n (<1) gives the degree of distortion from pure capacitor behaviour, i.e., $n = 1$ for the pure capacitor. The experimental spectra are shown as data points and fitted as continuous lines in Fig. 8. The total cell impedance is the summation of the electrolyte resistance (R_e), surface film impedance ($R_{(sf)}$) and the associated constant-phase element (CPE$_{(sf)}$), charge-transfer resistance ($R_{(ct)}$) and bulk resistance (R_b), the corresponding double-layer capacitance CPE$_{(dl)}$ and bulk capacitance (CPE$_b$), and the Warburg impedance, W. The evaluated values of the impedance parameters are given in Table 1.

The electrolyte resistance (R_e) was found to be 3.5($\pm$0.5) Ω at all voltages for both the first and tenth cycles. This shows that R_e is independent of the state-of-discharge–charge potential, as can be expected. The Nyquist plot of a fresh cell shows a semi-circle in the frequency range, 0.1 MHz to 25 Hz, followed by a Warburg region and an almost vertical line with an inclination of ~78° in the very low frequency region (Fig. 8a). This spectrum is fitted with a single semi-circle indicative of surface film impedance, $R_{(sf)} = 18(\pm5) \Omega$ and CPE$_{(sf)} = 244(\pm5) \mu$F. Such a low value of R_{sf} is surprising because it is almost an order of magnitude smaller than those measured in several other oxide anode materials [10,14,39]. The spectrum at 1.5 V does not show any change in the spread of semi-circle. The charge-transfer contribution has to be taken into account, however, and the data are fitted to yield $R_{(sf+ct)}$ and CPE$_{(sf+dl)}$. At 1.0 V, the spectrum shows a significant change and the spread of the semi-circle grows followed by an indication of the development of a second semi-circle. This significant change in the impedance marks the structure destruction reaction and the value of $R_{(sf+ct)}$ increases to 52($\pm$5) Ω, whereas CPE$_{(sf+dl)}$ decreases to 90($\pm$5) μF (Table 1). The second semi-circle, in frequency range, 8 Hz to 12 mHz, is indicative of the bulk impedance which is contributed by the composite electrode. The evaluated R_b is 50($\pm$5) Ω and the corresponding CPE$_b$ is 25($\pm$5) mF. In the voltage range of 0.75–0.05 V, $R_{(sf+ct)}$ and R_b vary in the range of (40–51)($\pm$5) Ω and the corresponding CPE values display a decreasing trend. This is the region where the Cd and Sn metals form the respective alloys (Eqs. (2) and (3)). At 0.005 V, $R_{(sf+ct)}$ and R_b increase to 49($\pm$5) Ω, and 60($\pm$5) Ω, respectively. The n value consistently increases from 0.74 at 1.0 V to 0.81 at 0.005 V.

Since the first charge process involves only the reverse reactions of Eqs. (2) and (3), it is different from first discharge process, and thus shows a different set of Nyquist plots. The data collected at 0.05–0.5 V were fitted using both the R||CPE circuit elements shown in Fig. 9. In the voltage range 0.05–0.50 V, the values of $R_{(sf+ct)}$
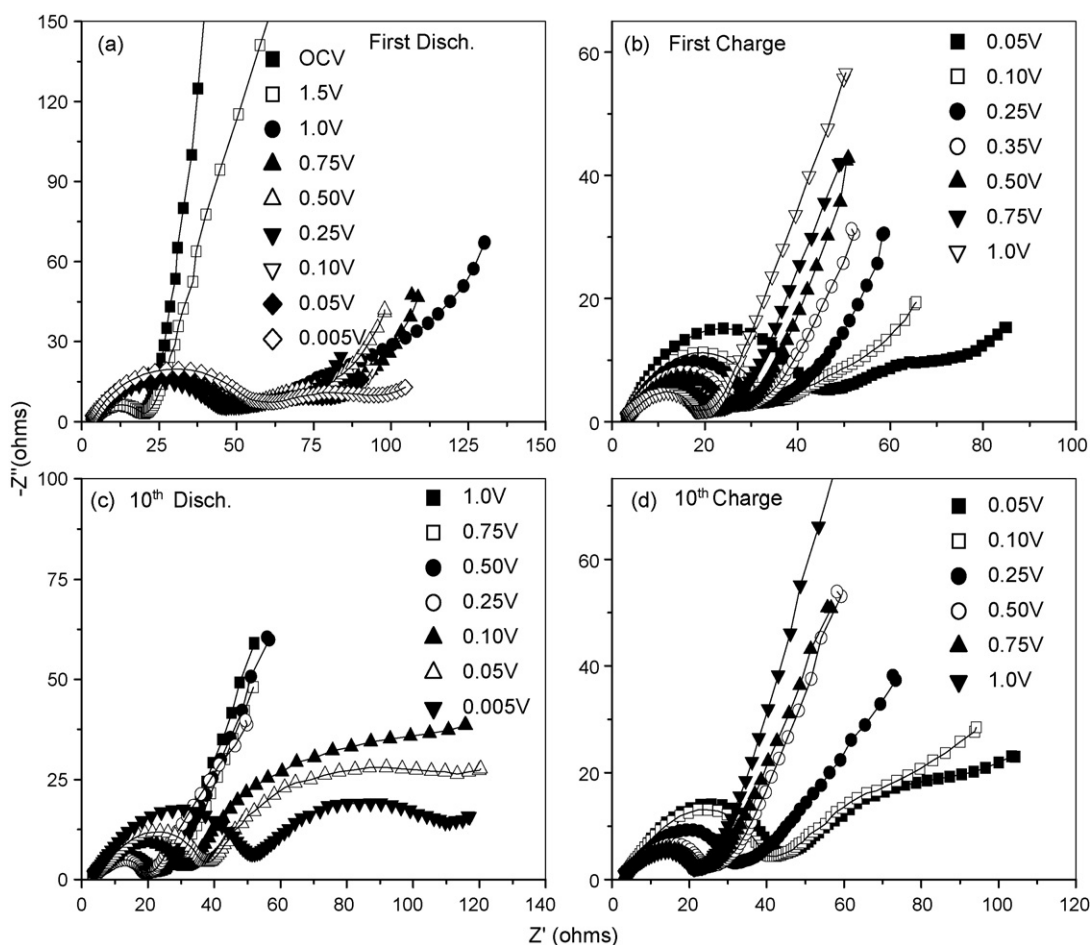
Fig. 8. Family of Nyquist plots (Z′ vs. −Z″) for nano-CdSnO$_3$–Li system at different voltages. (a) During 1st discharge reaction from open-circuit voltage (OCV ∼2.3 V). (b) During 1st charge reaction. (c) During 10th discharge cycle. (d) During 10th charge cycle. Voltages at which data are collected are shown. Symbols represent experimental data points and continuous lines show fitting with equivalent circuit of Fig. 9. Geometric area of electrode is ∼2 cm^2 and active mass in electrode is ∼3 mg.

and R_b consistently show a decrease, whereas the corresponding CPE$_{(sf+dl)}$ and CPE$_b$ show an increase (Table 1 and Fig. 8b). At 0.75 and 1.0 V, the Nyquist plots contain a single semi-circle followed by a Warburg-type region, which indicates that the contribution from R_b is negligible. The $R_{(sf+ct)}$ decreases from 22(±5) Ω at 0.75 V to 18(±5) Ω at 1.0 V. The n value shows a continuous decrease from 0.84 at 0.05 V to 0.57 at 1.0 V.

The Nyquist plots of the 10th discharge and charge are similar and match well with those of the first charge, thereby showing good reversibility of the system (Fig. 8c and d). According to the fitting, there are no noticeable changes in the Nyquist plots during the 10th discharge between 1.0 and 0.25 V, the latter is the average discharge potential of the nano-CdSnO$_3$–Li system. The spectra were fitted by a single R||CPE circuit element. The $R_{(sf+ct)}$ values are small and range

from 18(±5) Ω to 22(±5) Ω (Table 1). At 0.1 and 0.05 V, the $R_{(sf+ct)}$ increases to 29(±5) Ω along with the evolution of a second semi-circle in the mid-to-low frequency region, 13 Hz to 5 mHz, which reveals the contribution of the bulk impedance, R_b, that ranges from 102(±5) Ω to 113(±5) Ω. At 0.005 V, however, the $R_{(sf+ct)}$ increases to 47(±5) Ω whereas R_b decreases to 73(±5) Ω. The n value increases consistently from 0.53 at 1.0 V to 0.85 at 0.005 V.

During the 10th charge, the impedance spectra resemble those of the first charge, as can be expected. The impedance parameters $R_{(sf+ct)}$ and R_b are slightly higher in comparison with the first cycle, but the decreasing trend of these parameters with increase in charge voltage is clearly seen in the 10th cycle. Thus, the $R_{(sf+ct)}$ decreases from 33(±5) Ω to 22(±5) Ω in the range 0.05–1.0 V. The respective CPE$_{(sf+dl)}$ and CPE$_b$ increases with increase in voltage. The n value also decreases from 0.85 to 0.52 in the voltage range 0.05–1.0 V (Table 1 and Fig. 8d). It is concluded that the impedance spectral studies establish the electrochemical reversibility of the nano-CdSnO$_3$–Li system and corroborate the galvanostatic and cyclic voltammetry data.

3.4.1. Li-ion diffusion coefficient

Detailed analysis of impedance spectra can provide information regarding the chemical diffusion coefficient of the Li-ions (D_{Li^+}) involved in the electrode system. In the literature, the D_{Li^+} and its variation with the applied voltage as obtained from the impedance spectral analysis have been reported for systems consisting of thin films of Nb$_2$O$_5$–H [40,41] and LiCoO$_2$–Li [42] and polycrystalline LiCoO$_2$–Li [43,44], Co$_3$O$_4$ [45] and nano-CaO·SnO$_2$ [14]. The D_{Li^+} can
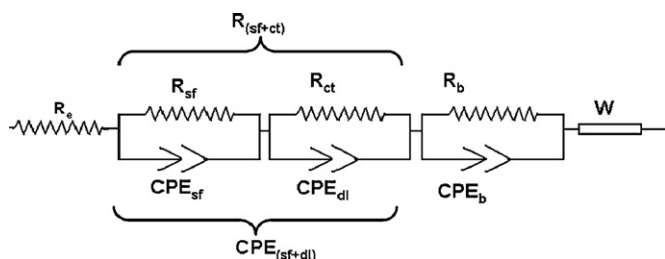

Fig. 9. (a) Equivalent circuit used for fitting impedance spectra of Fig. 8. Different resistances, R_i and/or R_i||CPE$_i$ components and Warburg element, W, are shown.

Table 1
Impedance parameters obtained by fitting impedance spectra of nano-CdSnO₃ (vs. Li) to equivalent-circuit elements during 1st and 10th cycle, and 'apparent' diffusion coefficients calculated using Eq. (5).

Voltage, V (vs. Li)	$R_{(sf+ct)}$, ($\pm$5) Ω	$CPE_{(sf+dl)}$, ($\pm$5) μF	R_b, ($\pm$5) Ω	CPE_b, ($\pm$5) mF	n ($\pm$0.01)	Frequency, f_L (mHz)	Diffusion coeff. (D_{Li^+}) (($\pm$0.05) $\times$ 10^{-13}) cm^2 s^{-1}
First discharge cycle							
OCV	18	244	–	–	0.70	–	–
1.50	18	157	–	–	0.74	–	–
1.00	52	90	50	25	0.72	10	2.8
0.75	51	70	45	21	0.74	8	2.3
0.50	45	70	43	23	0.74	12	3.4
0.25	40	58	40	23	0.76	12	3.4
0.10	44	52	45	19	0.79	–	–
0.05	44	51	44	21	0.79	–	–
0.005	49	44	60	18	0.81	–	–
First charge cycle							
0.05	35	44	50	28	0.84	–	–
0.10	27	57	30	44	0.85	–	–
0.25	27	111	20	47	0.83	10	0.10
0.35	19	112	10	52	0.75	20	0.15
0.50	21	200	5	70	0.72	25	0.20
0.75	22	550	–	–	0.57	100	0.80
1.00	18	670	–	–	0.57	100	0.80
10th discharge cycle							
1.00	21	850	–	–	0.53	100	0.80
0.75	22	717	–	–	0.60	80	0.62
0.50	22	680	–	–	0.54	60	0.50
0.25	18	515	–	–	0.52	–	–
0.10	29	218	113	55	0.65	–	–
0.05	28	70	102	27	0.85	–	–
0.005	47	47	73	17	0.85	–	–
10th charge cycle							
0.05	33	52	109	33	0.85	–	–
0.10	36	54	80	49	0.85	–	–
0.25	30	225	60	80	0.65	–	–
0.50	26	651	–	–	0.60	100	0.8
0.75	23	660	–	–	0.55	100	0.8
1.00	22	700	–	–	0.52	110	0.9

be estimated from the limiting frequency (f_L) using the following equation [14]:

$$D_{Li^+} = \pi L^2 f_L \qquad (5)$$

The parameter f_L is extracted from the impedance spectrum where the Warburg region (a straight line with a slope close to ∼45° from the real axis in the Nyquist plot) gives way to a vertical line, ∼80° on the real axis. This transition usually is realized at low frequencies ≤ 0.5 Hz. The L in Eq. (5) is the maximum length in the diffusion pathway in the electrode system. The film thickness in the case of thin film electrode and the average crystallite size of polycrystalline powder can be considered as the reasonable value of L in estimating the D_{Li^+}.

The f_L values were extracted from the spectra at various voltages for the nano-CdSnO₃–Li system in those cases where the transition from the Warburg region (semi-infinite diffusion process) to the near vertical line on the real axis (finite-length diffusion process) could be clearly delineated. The f_L values are listed in Table 1. The L value is taken as 30($\pm$5) nm during the first discharge, as established from Fig. 1 using Scherrer's equation. During the first charge and subsequent cycling, 'electrochemical grinding' of the particles take place due to volume changes occurring in the active material of the electrode. From Fig. 7a, it is noted that the crystallite size has been reduced from the initial value of 30 to ∼5 nm in size, and hence $L = 5$ nm is used to calculate D_{Li^+} during the first charge and during the 10th cycle.

It should be emphasized that Eq. (5) applies strictly to a single-phase discharge–charge process in the electrode system, whereas the alloying–de-alloying reactions involve two-phase reaction. Hence, the D_{Li^+} values in Table 1 must be considered as 'apparent'

chemical diffusion coefficients. Nevertheless, the relative variation in D_{Li^+} with applied voltage must represent the changes taking place in the system during lithium cycling. As can be seen from Table 1, during the first discharge to 1.0 V, the D_{Li^+} is 2.8×10^{-13} cm^2 s^{-1}. Upon further discharge to 0.75 V, the value decreases slightly to 2.3×10^{-13} cm^2 s^{-1}. This is due to the formation of metal nano-particles of Cd and Sn, followed by the onset of alloy formation, as established by galvanostatic and CV studies, and the onset of bulk impedance (R_b) below 1.0 V. There is, however, a gradual increase in D_{Li^+} from 2.3×10^{-13} to 3.4×10^{-13} cm^2 s^{-1} when the voltage decreases from 0.75 V → 0.5 V → 0.25 V (Table 1). This increase is due to the facile alloy-forming reaction (Li–Sn and Li–Cd) that occurs through several stages. At voltages 0.1, 0.05 and 0.005 V, the R_b masks the diffusion process and therefore, a clear cut transition frequency (f_L) is not observed.

During first charge, the D_{Li^+} is 0.1×10^{-13} cm^2 s^{-1} at 0.25 V, which is an order of magnitude smaller than that obtained during the first discharge. This is possibly due to a significant reduction in the crystallite size. The value increases from 0.1×10^{-13} to 0.8×10^{-13} cm^2 s^{-1} when the charging voltage is increased in steps from 0.25 to 1.0 V, respectively, corresponding to the de-alloying reactions, Eqs. (2) and (3). At voltages, $V \geq 0.5$ V, the D_{Li^+} lies in the range $(0.5–0.9) \times 10^{-13}$ cm^2 s^{-1} during the 10th cycle (Table 1). This indicates good lithium cycleability and complements the galvanostatic cycling and cyclic voltammetry data. The D_{Li^+} values during the 10th cycle, viz., $(0.5–0.9) \times 10^{-13}$ cm^2 s^{-1}, are almost an order of magnitude larger than those reported recently for the system nano-CaO·SnO₂–Li, namely, $\sim 1.0 \times 10^{-14}$ cm^2 s^{-1} (11th cycle values) [14]. This is understandable, since in the latter system, the CaO acts as an 'electro-inactive' matrix, whereas in the present nano-CdSnO₃–Li

system, the freshly formed nano particles of Cd are electro-active and alloy with Li. In both systems, Li_2O is formed during the first discharge process, Eq. (1) and Li_2O is an 'electro-inactive' matrix in the cycling voltage range, 0.005–1.0 V. The ratio of electro-active matrix elements to the electro-inactive matrix is 2:3 in the case of nano-CdSnO$_3$, whereas it is only 1:3 for nano-CaO·SnO$_2$. Hence a higher value of D_{Li^+} can be expected for the former system, as is presently observed. It is pertinent to mention that high values of D_{Li^+} ($\sim 1.0 \times 10^{-13}$ cm^2 s^{-1}) have been measured in thin films of the well-known cathode material LiCoO$_2$, in which the mechanism of lithium cycling involves de-intercalation–intercalation of Li ions in a two-dimensional lattice, and occurs essentially as a single-phase reaction [42]. In the present study, as mentioned earlier, lithium cycling occurs as two-phase reaction. It is concluded from EIS studies that the R_b dominates at low voltages (0.35 V), whereas $R_{(sf+ct)}$ and Warburg impedance dominate at higher voltages (0.35–1.0 V) during lithium cycling of nano-CdSnO$_3$. The apparent D_{Li^+} obtained from EIS is in the range of $(0.5–0.9) \times 10^{-13}$ cm^2 s^{-1} at 0.5–1.0 V during the 10th cycle.

4. Conclusions

Nano-CdSnO$_3$ is synthesized by the thermal decomposition of the precursor CdSn(OH)$_6$ at 600 °C for 6 h in air. The precursor is prepared by an aqueous co-precipitation method from salt solutions at ambient temperature. X-ray diffraction, HR-TEM and SAED analyses reveal a crystallite size of 30($\pm$5) nm. Galvanostatic cycling studies at room temperature and at 60 mA g^{-1} (0.13 C) are performed on nano-CdSnO$_3$ in two voltage windows, 0.005–1.0 V and 0.005–1.3 V versus Li. With the upper cut-off voltage of 1.0 V, nano-CdSnO$_3$ shows a reversible capacity of 475($\pm$5) mAh g^{-1} ($\sim$5 mol of Li per mole of CdSnO$_3$) which remains stable between 2 and 40 cycles with a coulombic efficiency, 97–98%. With the upper cut-off voltage of 1.3 V, the first charge capacity, 580($\pm$5) mAh g^{-1} degrades on cycling and is only 245($\pm$5) mAh g^{-1} after 25 cycles. Thus, a good voltage range for stable cycling response is 0.005–1.0 V.

The average discharge and charge reaction potentials are $\sim$0.2 and $\sim$0.4 V, respectively, as determined from the galvanostatic data and cyclic voltammetry. The impedance spectra during the 1st and 10th cycles are analyzed to evaluate the impedance parameters and the apparent chemical diffusion coefficient (D_{Li^+}). The bulk impedance, R_b, dominates at low voltages ($\leq$0.25 V), whereas the surface film and charge-transfer impedance ($R_{(sf+ct)}$) along with the Warburg impedances dominate at $\geq$0.25 V. The value of D_{Li^+} is in the range of $(0.5–0.9) \times 10^{-13}$ cm^{2}s^{-1} at 0.5–1.0 V during the 10th cycle.

The proposed reaction mechanism involves de-alloying and alloying reactions of both Cd and Sn with Li that contribute to the reversible capacity. This is well supported by ex situ XRD, TEM and SAED studies. Favourable charge and discharge potentials with low hysteresis, and a stable capacity higher than the theoretical capacity of graphite (372 mAh g^{-1}) justify the suitability of nano-CdSnO$_3$ as an anode material for LIBs. The observed capacity of 475($\pm$5) mAh g^{-1}, which is lower than the theoretically expected value of 710 mAh g^{-1}, and the toxicity of Cd are the main concerns that may be addressed to some extent by tailoring the particle morphology and by replacing Cd by other eco-friendly metals, respectively.

References

[1] G.A. Nazri, G. Pistoia (Eds.), Lithium Batteries: Science and Technology, Kluwer Academic, New York, 2003.
[2] N. Takeda, S. Imai, Y. Horri, H. Yoshida, Mitsubishi Motors Tech. Rev. 15 (2003) 68.
[3] M. Armand, J.-M. Tarascon, Nature 451 (2008) 652.
[4] J.L. Tirado, Mater. Sci. Eng. R 40 (2003) 103.
[5] A.K. Shukla, T.P. Kumar, Curr. Sci. (India) 94 (2008) 314.
[6] Y.-G. Guo, J.-S. Hu, L.-J. Wan, Adv. Mater. 20 (2008) 2878.
[7] Y. Idota, T. Kubota, A. Matsufuji, Y. Maekawa, T. Miyasaka, Science 276 (1997) 1395.
[8] Y. Sharma, N. Sharma, G.V. Subba Rao, B.V.R. Chowdari, J. Mater. Chem., submitted for publication.
[9] P. Poizot, S. Laruelle, S. Grugeon, L. Dupont, J.-M. Tarascon, Nature 407 (2000) 496.
[10] Y. Sharma, N. Sharma, G.V. Subba Rao, B.V.R. Chowdari, Solid State Ionics 179 (2008) 587.
[11] Y. Yu, C.-H. Chen, J.-L. Shui, S. Xie, Angew. Chem. Int. Ed. 44 (2005) 7085.
[12] Y. Sharma, N. Sharma, G.V. Subba Rao, B.V.R. Chowdari, Adv. Funct. Mater. 17 (2007) 2855.
[13] G. Derrein, J. Hassoun, S. Panero, B. Scrosati, Adv. Mater. 19 (2007) 2336.
[14] Y. Sharma, N. Sharma, G.V. Subba Rao, B.V.R. Chowdari, Chem. Mater. 20 (2008) 6829.
[15] F. Cheng, Z. Tao, J. Liang, J. Chen, Chem. Mater. 20 (2008) 667.
[16] Z. Wen, Q. Wang, Q. Zhang, J. Li, Adv. Funct. Mater. 17 (2007) 2772.
[17] C. Kim, M. Noh, M. Choi, J. Cho, B. Park, Chem. Mater. 17 (2005) 3297.
[18] A. Timmons, J.R. Dahn, J. Electrochem. Soc. 153 (2006) A1206.
[19] N. Sharma, K.M. Shaju, G.V. Subba Rao, B.V.R. Chowdari, Electrochem. Commun. 4 (2002) 947.
[20] I.A. Courtney, J.R. Dahn, J. Electrochem. Soc. 144 (1997) 2943.
[21] M. Behm, J.T.S. Irvine, Electrochim. Acta 47 (2002) 1727.
[22] P.A. Connor, J.T.S. Irvine, J. Power Sources 97–98 (2001) 223.
[23] F. Belliard, P.A. Connor, J.T.S. Irvine, Solid State Ionics 135 (2000) 163.
[24] F. Belliard, J.T.S. Irvine, J. Power Sources 97–98 (2001) 219.
[25] N. Sharma, J. Plevert, G.V. Subba Rao, B.V.R. Chowdari, T.J. White, Chem. Mater. 17 (2005) 4700.
[26] N. Sharma, K.M. Shaju, G.V. Subba Rao, B.V.R. Chowdari, J. Power Sources 139 (2005) 250.
[27] I.A. Courtney, J.R. Dahn, J. Electrochem. Soc. 144 (1997) 2045.
[28] A. Rong, X.P. Gao, G.R. Li, T.Y. Yan, H.Y. Zhu, J.Q. Qu, D.Y. Song, J. Phys. Chem. B 110 (2006) 14754.
[29] J. Wang, P. King, R.A. Huggins, Solid State Ionics 20 (1986) 185.
[30] T. Zhang, Y. Shen, R. Zhang, Mater. Lett. 23 (1995) 69.
[31] Y.-L. Liu, Y. Xing, H.-F. Yang, Z.-M. Liu, Y. Yang, G.-L. Shen, R.-Q. Yu, Anal. Chim. Acta 527 (2004) 21.
[32] Y. Tang, Y. Jiang, Z. Jia, B. Li, L. Luo, L. Xu, Inorg. Chem. 45 (2006) 10774.
[33] G. Raynor, J.A. Lee, Acta Metall. 2 (1954) 616.
[34] G.C. Che, M. Ellner, K. Schubert, J. Mater. Sci. 26 (1991) 2417.
[35] S.T. Chang, I.C. Leu, C.L. Liao, J.H. Yen, M.H. Hon, J. Mater. Chem. 14 (2004) 1821.
[36] M. Mohamedi, S.-J. Lee, D. Takahashi, M. Nishizawa, T. Itoh, I. Uchida, Electrochim. Acta 46 (2001) 1161.
[37] Y. Li, B. Tan, Y. Wu, Chem. Mater. 20 (2008) 567.
[38] D. Aurbach, A. Nimberger, B. Markovsky, E. Levi, E. Sominski, A. Gedanken, Chem. Mater. 14 (2002) 4155.
[39] Y.M. Kang, M.-S. Song, J.-H. Kim, H.-S. Kim, M.-S. Park, J.-Y. Lee, H.K. Liu, S.X. Dou, Electrochim. Acta 50 (2005) 3667.
[40] R. Cabanel, J. Chaussy, J. Mazuer, G. Delabouglise, J.C. Joubert, G. Barral, C. Montella, J. Electrochem. Soc. 137 (1990) 1444.
[41] R. Cabanel, G. Barral, J.-P. Diard, B.L. Gorrec, C. Montella, J. Appl. Electrochem. 23 (1993) 93.
[42] J. Xie, N. Imanishi, T. Matsumura, A. Hirano, Y. Takeda, O. Yamamoto, Solid State Ionics 179 (2008) 362.
[43] B. Garcia, J. Farcy, J.P. Pereira-Ramos, N. Baffier, J. Electrochem. Soc. 144 (1997) 1179.
[44] P.-J. Cho, E.-D. Jeong, Y.-B. Shim, Bull. Kor. Chem. Soc. 19 (1998) 39.
[45] Y. Liu, C. Mi, L. Su, X. Zhang, Electrochim. Acta 53 (2008) 2507.